Insight on oxidation process and wettability of femtosecond laser ablated Ti surfaces

Ilemona S Omeje, Djafar Iabbaden, Patrick Ganster, Tatiana E Itina

Insight on oxidation process and wettability of femtosecond laser ablated Ti surfaces

Ilemona S. Omeje*[1], Djafar Iabbaden[2], Patrick Ganster[3], and Tatiana E. Itina[1]

[1] *Univ Lyon, UJM-Saint-Etienne, CNRS, IOGS, Laboratoire Hubert Curien UMR5516, F-42023 St-Etienne, France*

[2] *LEM3, CNRS – Université de Lorraine – Arts et Métiers ParisTech, 7 rue Félix Savart, 57070 Metz, France*

[3] *Laboratoire Georges Friedel, Ecole des Mines, Saint-Etienne, France*

Abstract

xxxxxxxx

1 Introduction

The surface properties of materials play a crucial role in various industrial applications ranging from biomedicine to aerospace engineering. Among these properties, wettability, which determines the interaction between a liquid and a solid surface, holds significant importance. Understanding and controlling wettability is particularly essential in fields like biomaterials, where surface interactions dictate biological responses such as cell adhesion and protein absorption.

Femtosecond laser surface treatment has attracted significant attention in recent years due to its numerous advantages over traditional surface modification techniques []. Particularly, such lasers operate with extremely short pulses in the order of femtoseconds, allowing for precise control over material processing at the micro- and nanoscale. This level of precision enables tailored modification of surface properties with high spatial resolution, making it ideal for applications requiring intricate surface patterning or functionalization. Furthermore, unlike conventional laser processing methods, femtosecond lasers induce minimal heat-affected zones (HAZ) during surface treatment and they are applicable to a wide range of materials []. This versatility stems from the ability to tailor laser parameters such as pulse duration, energy, and repetition rate to suit the specific material properties and desired surface modifications. As a result, femtosecond lasers offer a versatile platform for surface engineering across diverse industrial sectors, from aerospace and electronics to biomedicine and photovoltaics []. Additionally, femtosecond laser treatment often eliminates the need for extensive post-processing steps such as chemical etching or coating deposition, which are commonly required in conventional surface modification techniques. The direct and precise nature of femtosecond laser-induced surface alterations can achieve desired functionalities, such as enhanced wettability and biocompatibility, without additional processing steps, thereby streamlining manufacturing processes and reducing production costs. Finally, femtosecond lasers can achieve high processing speeds due to their high repetition rates and efficient energy delivery mechanisms. This enables rapid surface modification over large areas with minimal dwell time, making femtosecond laser treatment suitable for high-throughput manufacturing applications.

Molecular dynamics (MD) simulations offer a powerful tool to investigate the intricate processes occurring at the atomic scale, providing insights that complement experimental observations. In this context, the present study endeavors to delve into the early stages of oxidation effects on the wettability of femtosecond laser-treated Ti surfaces using MD simulations.

The early oxidation phenomena play a pivotal role in determining the subsequent surface properties in both metallic and amorphous materials, yet they are often challenging to observe experimentally due to their transient nature [1, 2]. By employing MD simulations, we aim to unravel the intricate interplay between laser-induced surface modifications, oxygen adsorption, and subsequent oxide formation, shedding light on the dynamic evolution of surface wettability.

This article presents a numerical study of the temporal evolution of laser irradiated morphology, chemical composition, and wettability characteristics of femtosecond laser-treated Ti surfaces under varying oxidation conditions [3]. Through rigorous computational analyses, we seek to elucidate the fundamental mechanisms governing the observed changes in surface wettability, thus providing valuable insights for optimizing the design and performance of laser-treated Ti surfaces in diverse technological applications.

2 Simulations details

This section focuses on the various simulations conducted to investigate the wetting properties of the ti-

*Corresponding author: ilemona.sunday.omeje@univ-st-etienne.fr

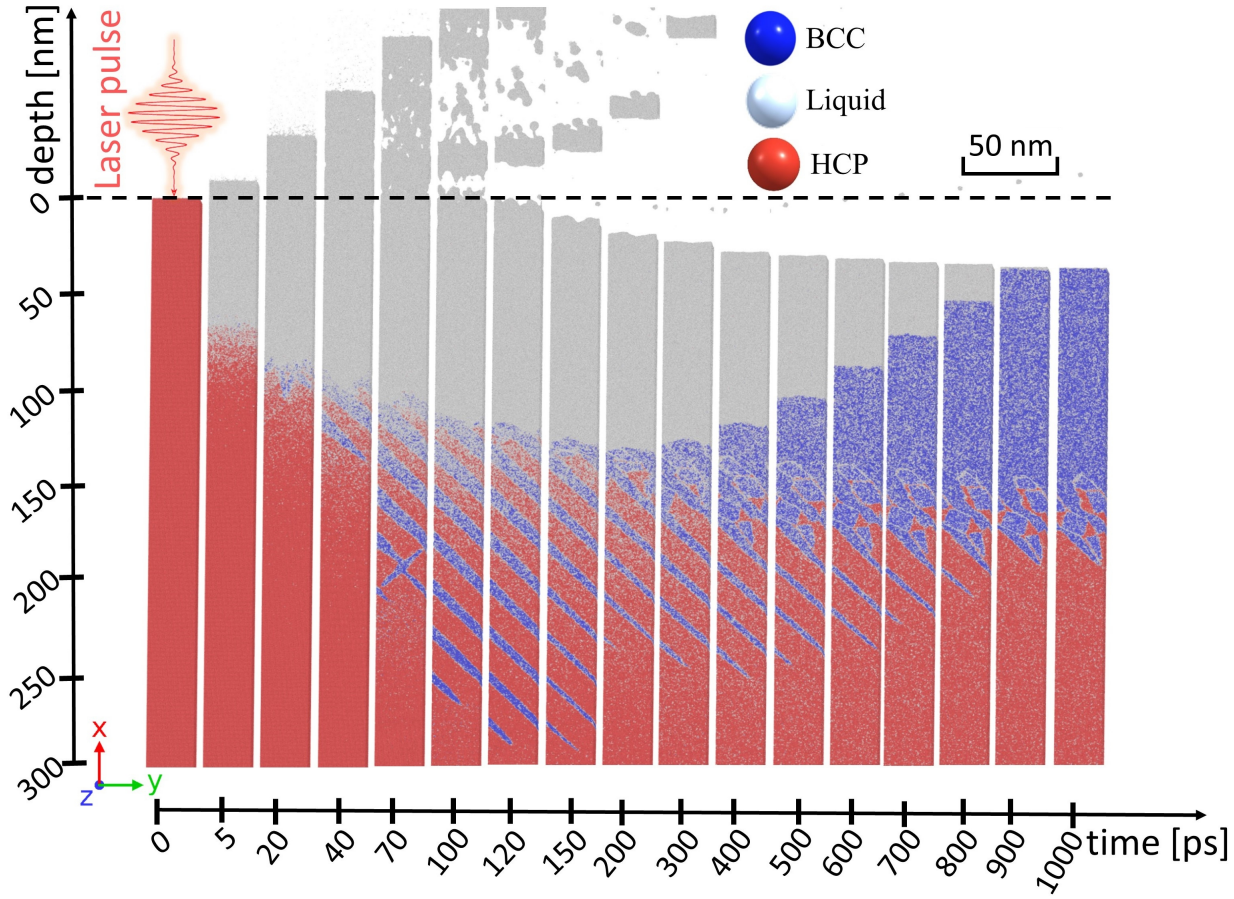

Figure 1: Snapshots of Ti local atomic structure evolution during ultrafast laser energy deposition at t=0, 5, 20, 40, 70, 100, 120, 150, 200, 300, 400, 500, 600, 700, 800, 900, and 1000 ps. The irradiation conditions of F_0=300 mJ/cm^2, and t_p=500 fs are used for absorbed fluence and pulse duration respectively. The atoms are colored according to their local atomic structure computed using the CNA (Common Neighbor Analysis) algorithm. The black dashed line in the upper part of target correspond to the position of the initial surface.

tanium surface. The interaction between a laser and Ti surface is primarily modeled using a combination of Molecular Dynamics (MD) and the Two Temperature Model (TTM). Subsequently, after the laser energy deposition crystallizes the surface, a specific region of interest is extracted to serve as the initial block for the oxidation investigation. Finally, the droplet model is employed to examine the surface wettability.

2.1 Laser-matter interaction for surface preparation

To understand the influence of ultrafast laser on oxidation processes within Ti surfaces from a pure theoretical perspective. We first started preparing the irradiated surface using a hybrid approach that combines MD-TTM introduced by Anisomov *et al* [4] as implemented in LAMMPS package [5, 6]. Initially, we started building a Hexagonal Close Packed (HCP) Ti cell of dimensions of 0.295 × 0.511 × 0.469 nm^3 having an orientation of [0-110] [10-10] [0001] using ATOMSK [7]. This structure was replicated to construct a supercell with a realistic size of L_x × L_y × L_z=885.0 × 20.4 × 18.7 nm^3. A segment of 354.0 and 88.5 nm is removed from the left and right sides along L_x of this supercell respectively. Thereby, a structure equivalent to 9600000 atoms filling a space of 442.5 × 20.4 × 18.7 nm^3 atoms will be used for laser-matter simulation. A TTM-MD hybrid model requires knowledge of nonequilibrium coefficients, namely the electron specific heat ($C_e(T_e)$), electron-phonon coupling factor ($G_e(T_e)$), and electronic thermal conductivity ($\kappa_e(T_e)$). Therefore, we collected the property of $C_e(T_e)$ from the first principles calculations as described by *Bévillon et al* [8], $G_e(T_e)$ is as estimated by *Lin et al* [9], and $\kappa_e(T_e)$=$\kappa_0 \frac{T_e}{T_l}$ is computed using a linear approximation [10], where κ_0=22.3 W m^{-1} K^{-1} at T_0=300 K as reported in the work of Uher *et al* [11]. The laser energy is deposed following a Gaussian shape function in time multiplied by an exponentially decreasing in space. The source term $S(x,t)$ is described as :

$$S(x,t) = \left(\frac{2F}{l_p t_p}\sqrt{\frac{ln(2)}{\pi}}\right) e^{-4ln(2)\frac{(t-t_0)^2}{t_p^2}} e^{-x/l_p} \quad (1)$$

where t_p represents the pulse duration, t_0, $lp(T_e)$ correspond to the maximum time of the laser pulse at the surface of the target, and laser penetration depth respectively. The F is defined as the absorbed fluence, defined by F=$F_0[1 - R(T_e)]$ with F_0

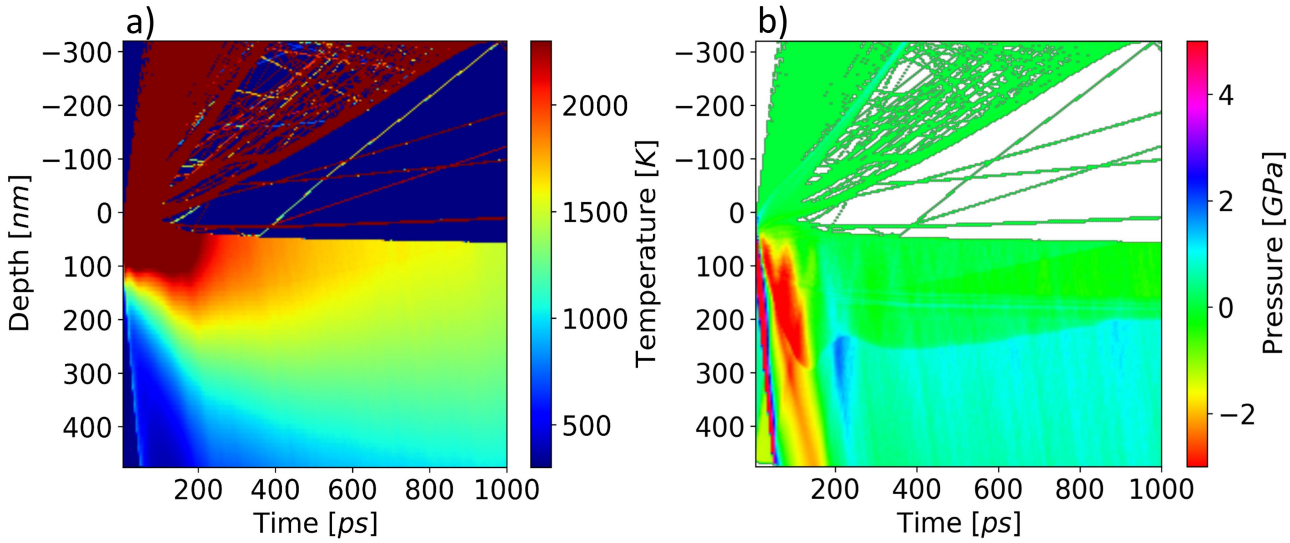

Figure 2: Spatiotemporal maps showing the evolution of thermodynamic quantities at different transformed regions: a) lattice temperature, and b) pressure. The initial surface position is set at 0 nm. An absorbed laser fluence of 300 mJ/cm^2 and a pulse duration of 500 fs are used.

being the incident fluence and $R(T_e)$ being the reflectivity as computed in the work of Bévillon *et al* [12].

A free boundary follows laser propagation direction, namely x, while periodic boundaries are set for both y and z. Actually, the simulation domain is divided into two distinct regions: the TTM-MD domain where the TTM and MD equations are solved simultaneously on a mesh of $100 \times 3 \times 3$, and the TTM region (bulk) with a thickness of 0.9 μm where only TTM equations are solved on a grid of $90 \times 1 \times 1$ large enough to ensure heat dissipation. These TTM-MD and TTM regions are separated by an Absorbing Boundary Condition (ABC) as described in the work of Schäfer *et al* [13] that is positioned at the rear part of the TTM-MD atomic domain to avoid the pressure wave reflection during the laser energy deposition. The ABC region thickness is ∼9.50 Å, characterized by a damping coefficient α=0.03 eV/Å^3. The Ti supercell is equilibrated at 300 K within the microcanonical ensemble (NVE) during 60 ps. The laser-matter interaction operation conditions namely pulse duration and fluence are chosen to be similar to the experimental work of Cunha *et al* [14] where t_p=500 fs and F_0=300 mJ/cm^2 are considered. After the laser energy is deposed, the thermodynamics evolution of the system is monitored for 1 ns. An MD integration time step of δt=1 fs is employed throughout all the TTM-MD simulations, the Embedded Atom Method (EAM) interatomic potential developed by Mendelev *et al* [15] is used, and the local atomic structures post-process analysis is performed with OVITO software [16].

2.2 Reactive molecular dynamics

The oxidation process of laser-irradiated Ti is investigated using the reactive force field (ReaxFF) [17, 18]. ReaxFF offers a more precise representation of chemical reactions by incorporating bond breaking and formation through the calculation of bond orders based on inter-atomic distances. Details of the ReaxFF can be found in [17–19]. The ReaxFF potential used in this study were developed by Kim et al. [20] and this inter-atomic potential was designed to specifically describe the interactions between T/O/H. These potential have been recently applied to describe the TiO_2 Nanocrystals growth [21] and other interesting system [22], which shows the validity of the potential.

a segment of 23.3 × 51 × 27 nm^3, containing 4492 atoms, was obtained from the equilibrated Ti before laser irradiation. Similarly, a dimension of 36 × 51 × 47 nm^3, equivalent to 4388 atoms, was extracted from the laser-irradiated Ti surface. Additionally, a 20 nm vacuum was added along the x-axis of both slabs to accommodate O_2 molecules. Subsequently, 1000 O_2 molecules were randomly distributed onto both slabs, resulting in 6492 atoms for Ti system and 6388 atoms for the laser-irradiated Ti surface as shown in Appendix **??**.

Periodic boundary conditions were implemented along the y and z directions, while the x direction was set as non-periodic to prevent undesired oxidation on the bottom of the Ti. The simulation was conducted at a room temperature of 300 K, utilizing a Berendsen thermostat with a temperature-damping constant of 1 fs. A time step size of 0.25 fs was employed, and the oxidation process lasted for 1 ns. The simulation was performed using a microcanonical ensemble (NVE). Additionally, atomic coordinates and atom types were saved every 10000 time steps throughout the simulation.

3 Results and discussion

This section presents the findings of our simulations, which examine the effects of laser interaction with a bulk Ti target. The simulations are conducted using a pulse duration of 500 ps and an absorbed laser

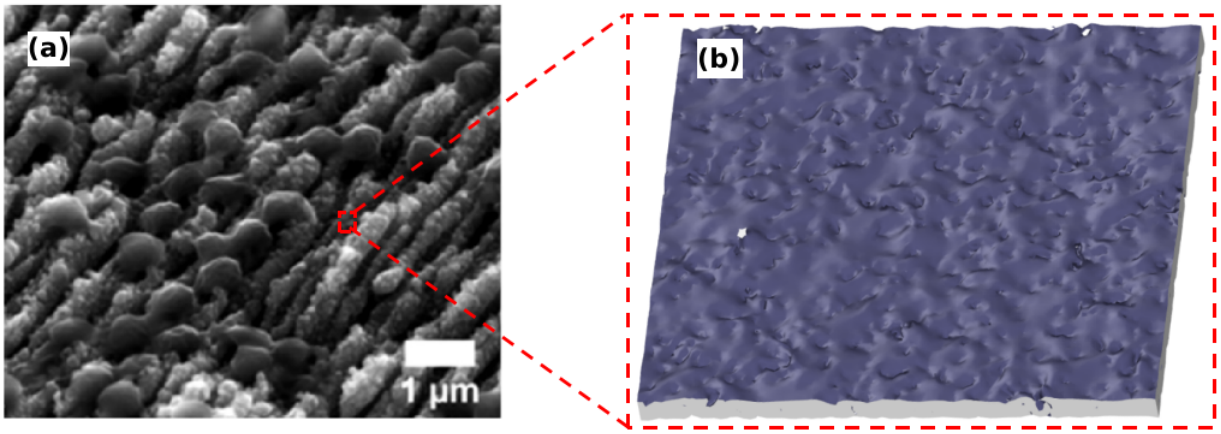

Figure 3: Spatiotemporal color maps showing the evolution of thermodynamic quantities in the hexagonal Ti in different transformed regions : a) lattice temperature, and b) pressure. The initial surface position is set at 0. An absorbed laser fluence of 300 mJ/cm^2 and a pulse duration of 500 fs are used.

fluence of 300 mJ/cm^2, corresponding to the experimental laser parameters of [14]. We investigate the interfacial energies and the early oxidation process of laser-irradiated Ti surfaces. We discuss the relationship between interfacial surface energies and the early oxidation of the laser-irradiated surfaces. A series of wetting simulation tests is conducted on the surfaces to gain insights into the influence of surface chemistry on the observed changes in the wetting behavior of laser-irradiated Ti.

3.1 Melting and resolidification of laser irradiated Ti

Figure 1 shows the evolution of Ti HCP microstructure after the ultrafast laser irradiation, where only a certain zones of interest where interesting transformations are occurring. The evolution of local structure is investigated by applying the CNA algorithm to detect perfect HCP crystal structure and transformed domains into BCC and liquid phases. Instantaneously after energy deposition at t=5 ps, the upper part of the target ∼90 nm deep in the material is completely melted, this melting front reaches its critical depth when the resolidification process is initiated at t=150 ps for a value of x∼123 nm as shown by atoms in grey. Concomitantly, we notice a rapid expansion of this melted part beyond the initial position of the surface. This results on formation of several nanovoids at t=70 ps, this process let place to ablation regime where this part is completely torn off in the form of a thick layer of atomic planes, nanoparticles, and debris with different sizes. In the same time at t=40 ps, a BCC crystalline phase starts nucleates within the liquid-solid interface at x∼93 nm and then propagates far deep inside the material to reach a critical propagation at t=150 ps for x∼270 nm. The initial transformed domain at t=40 ps takes the form of a nano-blade of ∼12 nm thickness and as soon as the nano-blades propagates across the sample due to periodic boundary condition following the lateral sides y-z the thickness drops to 2 nm. The spatial distribution of these nano-blade follow a pseudo-periodic pattern separated by a thin HCP structure slices of thickness ∼16 nm. A closer look to the transformed BCC phase confirmations that the structure is nanotwinned and propagates following the relative orientation $\{11\bar{2}0\}$ with respect to the initial crystal orientation.

Indeed, Beyond the key time of t=150 ps, we notice that the propagation of BCC nano-blades stops and the local melted part starts to transform from liquid to a BCC-like structure with presence of point defects shown in gray marking the beginning of resolidification process. Meanwhile, at t=150 ps the twinned nano-blades experience instabilities thereby they disappear at t=1000 ps except at the BCC-like-HCP interface where a nano-blade survives. The resolidification is characterized here by the propagation of crystallisation front that appears within the time range of t=150-1000 ps leading to a full crystallization of the liquid part to BCC-like phase. To correlate pressure, and temperature role in the comprehension of all these phase transformations, a spatio-temporal evolution of these properties are depicted in Figure 3.

Figure 3(a) shows that after the deposition of the energy we have an increase of lattice temperature up to ∼2500 K above the theoretical melting temperature T_m=1150 K provided by the interatomic potential. Since this temperature reached at these laser conditions is ∼2T_m, ablation processes takes place. Moreover, as mentioned previously the removed layers, debris are in a complete liquid phase. Meanwhile, at subsurface going from x∼150-270 nm, the HCP is strongly perturbed by not enough to induce melting of the system since an average temperature of at t>150 ps is ∼1000 K is recorded which is below the T_m. Therefore, the observed nano-twinned blades are mainly due to pressure effects. The evolution of pressure profile is shown in Figure 3(b). The temperature gradients due to the laser energy deposition induce the production

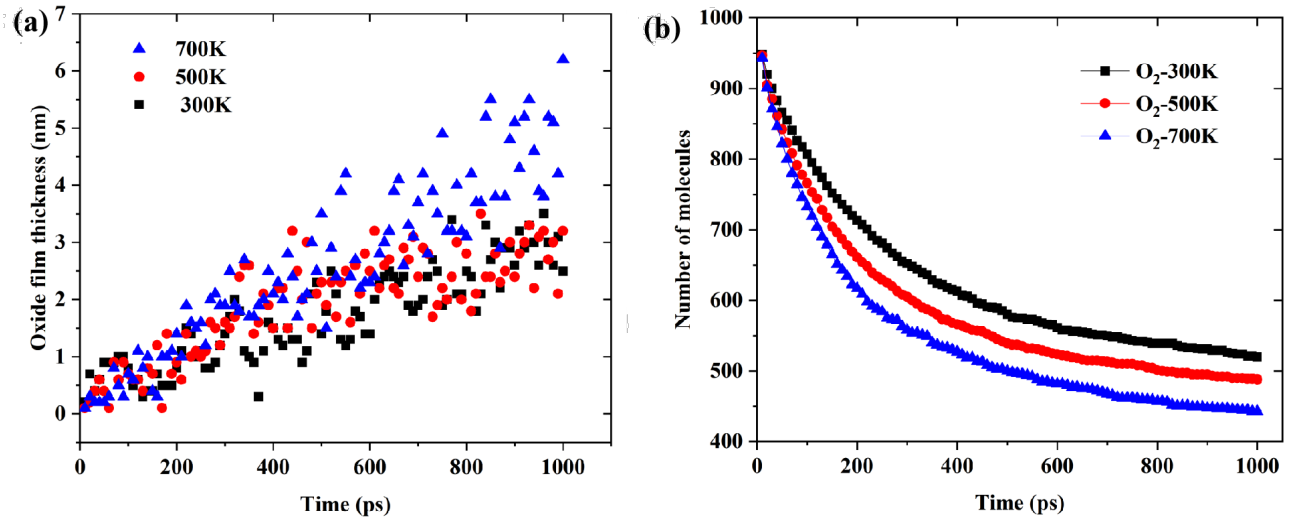

Figure 4: (a) Growth of the oxide film as a function of time; (b) Evolution of the number of molecules of O_2 , during the oxidation of Ti at 300K, 500k and 700K.

of compression shock wave, followed by a rarefaction wave with positive and negative front respectively. At t∼0-40 ps, the passage of the compression wave with a maximum head value of ∼ 5 GPa distort the region but did not instigate any phase transformation. On the other hand, at t∼40-150 ps the transformed region undergoes the passage of the rarefaction wave with a maximum value ∼−3 GPa this coincide exactly with the formation BCC nanotwinned blades. It important to notice that at t>150 ps, due to resolidification process the pressure conditions is alternated where a positive pressure appear with a extremum value of ∼2 GPa that affects the stability of the previously formed BCC nanotwinned blades causing the cessation of twinning.

3.2 Oxidation of non-irradiated Ti and laser-irradiated Ti

Ti is a highly reactive metal, and understanding its oxidation behavior at various temperatures is essential. To investigate this process, we conducted reactive molecular dynamics simulations using the ReaxFF force field to study the early of oxidation process on pure Ti. Given that Ti typically undergoes parabolic oxidation within the 873–1173 K temperature range [23], where the oxide layer growth rate slows down as the layer thickens, we chose lower temperatures (300 K, 500 K, and 700 K) to enable finer control over oxidation kinetics and oxide layer development in our simulations. In addition, oxidation of laser-irradiated Ti was simulated at room temperature (300 K) for comparison with the 300 K oxidation process of untreated Ti.

Fig. 4 (a) shows the oxide film thickness as a function of time on Ti, and Fig. 4 (b) shows evolution of the number of moles of oxygen during the oxidation of ti at 300, 500 and 700K. In Fig. 4 (a), the obtained results for non-irradiated Ti indicate that the thickness of the oxide layer increases over time. This growth of the TiO_x layer is not uniform throughout the simulation period. Initially (300–1000 ps), the layer exhibits more rapid growth compared to the earlier stages (0–300 ps) and this observe across different temperatures (300K, 500K, and 700K). The temperature variation notably influences the growth kinetics of the oxide layer. At higher temperatures (500K and 700K), the initial growth of the TiO_x layer is more pronounced compared to that observed at 300K. This suggests that increased temperatures accelerate the initial oxide layer formation on the Ti surface.

Figure 5 presents the Radial Distribution Function (RDF), which describes how atomic density varies with distance, of the oxide layer on Ti at at 300, 500 and 700K in comparison to the reference experimental RDF of pure Ti. The RDF offers insights into the characteristics of the oxide layer formed on the Ti surface at each temperature. In Fig. 5(a)...

In Fig. 4 (b), the thickness changes in the TiO_x layer correspond inversely with the diffusion of O_2 molecules. During the initial stages (0–300 ps), the increase in the TiO_x layer thickness is accompanied by a decrease in O_2 diffusion. However, in the later stages (300–1000 ps), as the growth rate of the TiO_x layer diminishes, there is an observed increase in O_2 diffusion. At a higher temperature of 700K, the oxide layer remains relatively thin, approximately measuring around 4 nm. This thinness might indicate a more rapid consumption or reaction of O_2 with the Ti surface at this increased temperature. It's evident that the consumption of O_2 by the Ti surface is notably higher at 700K compared to the lower temperatures of 300K and 500K. This suggests a more active interaction between O_2 molecules and the Ti surface at higher temperatures, contributing to faster oxide growth [**?**].

Figure 5 (a) and (b) shows the oxide film thickness and the number of molecules of O_2 during the oxidation on Ti and laser-irradiated Ti at a room temperature of 300K. This oxidation study was specifically performed at room temperature to replicate experimental conditions and environmental factors. Our results distinctly

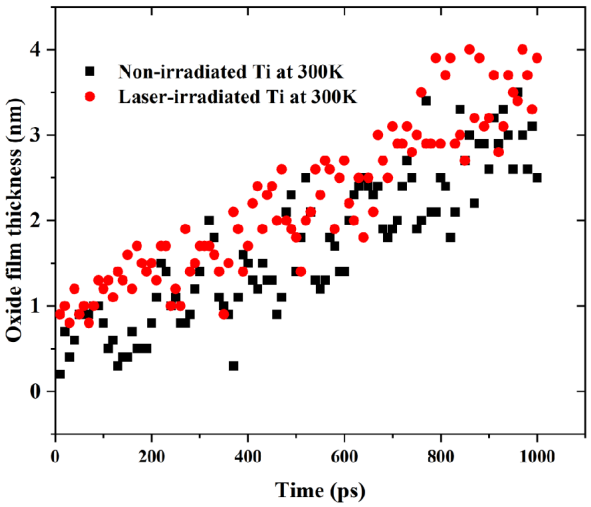

Figure 5: (a) Normalized thickness of oxide layer on titanium and laser-irradiated titanium at room temperature (300K). (b) The number of molecules of O_2 during the oxidation of Ti at 300K.

reveal that laser irradiation significantly affects the oxidation process of Ti. It can be clearly seen that oxide film thickness for laser-irradiated Ti is 4 nm and that of non-irradiated Ti is 3 nm. The observed difference in oxide thickness between the two systems ranges from 0.5 to 1 nm. This variation in oxide thickness can be attributed to the defects induced by laser treatment on Ti, creating an increased affinity for O_2 molecules [**?**]. The defects induced by laser treatment can serve as active sites for oxygen adsorption or diffusion onto the Ti surface. These defects create additional reactive sites, effectively increasing the surface area available for interaction with O_2 molecules [**?**]. As a consequence of this, the availability of these defect sites facilitates a more rapid interaction between the Ti surface and oxygen molecules. This enhanced reactivity accelerates the initial stages of oxide layer formation, leading to a relatively thicker oxide layer compared to non-irradiated Ti.

In addition, experimental findings suggest that immediately after laser irradiation, the laser-treated surface exhibits hydrophilic behavior, gradually changing to a hydrophobic state over time. From our calculations, we can infer that the development of the oxide layer, influenced by the defects induced by laser treatment, contributes to the hydrophobic behavior observed in the laser-treated surface. This oxide layer, formed due to increased reactivity with O_2, modifies the surface properties, making it less favorable for interactions with water molecules. In addition, the increasing oxide thickness over time, a consequence of enhanced reactivity induced by defects, could potentially lead to a larger contact angle. As the oxide layer grows, it modifies the surface properties further, contributing to a more hydrophobic surface and an increased contact angle with water droplets. Therefore, our calculations shed light on the early oxidation processes of both Ti and laser-irradiated Ti, providing insights into how these evolving behaviors affect the wettability of laser-treated surfaces.

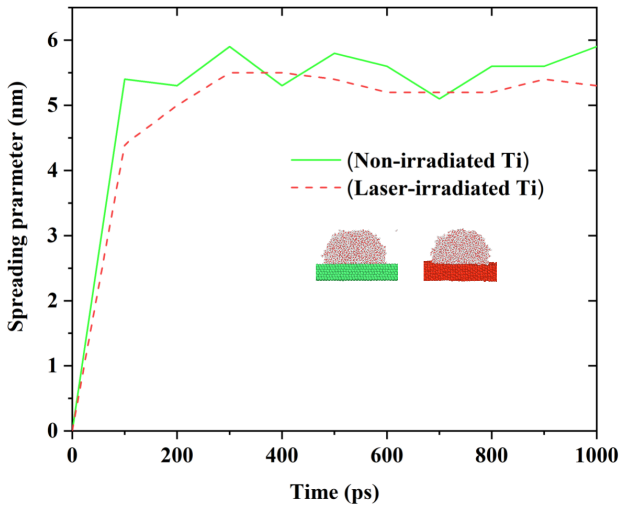

Figure 6: Spreading radius of water nanodroplet on non-irradiated and laser-irradiated titanium.

3.3 Droplet model

The water droplet on the laser-irradiated Ti surface is simulated using the Simple Point Charge/Extended (SPC/E) model for water [24]. The entire Molecular Dynamics (MD) calculation is conducted in LAMMPS. The interaction between water molecules and the laser-irradiated Ti surface is described using a 12-6 Lennard-Jones (L-J) potential and a long-range electrostatic potential. Notably, the same droplet model and LJ parameters utilized in the previous chapter (as detailed in **??**) are consistently applied throughout the wetting studies.

The laser-irradiated Ti slab, obtained from the laser-ablated Ti, has a dimension of 17.0 × 20.4 × 18.7 nm^3 and contains 27,340 atoms. The relaxed SPC/E water, obtained in the previous chapter, was subsequently positioned on the laser-ablated Ti slab, totaling 33,220 atoms, as shown in Appendix **??**. For simulating the water droplet on the laser-irradiated Ti, periodic boundary conditions were applied along the xyz axis. To optimize computational efficiency, the laser-irradiated Ti surface was kept fixed. Following this, a Nose-Hoover thermostat (NVT) at 300K was utilized with a time step of 1 fs for a duration of 1 ns. The determination of the contact angle of the water droplet on the surfaces followed the same methodology detailed in previous chapter.

3.4 Wettability of Ti and laser-irradiated Ti

It has been shown in the previous chapter (**??**) that our MD water model captures the evolution of water droplets on non-irradiated Ti. The equilibrium contact angle (ECA) was shown to be 54°, which is in close agreement with the experimental observations of

50° ± 6° reported by others including Cunha et. al. [14]. However, the ECA of laser-irradiated Ti from our MD simulation is 85° and that of the experiment is 12° ± 3.1°. There is a great disagreement between ECA of our MD simulation and that of the experiment with a difference of ∼ 73°. Our MD simulation indicates a more hydrophilic wettability, whereas the experimental observation is hydrophilic — a trend commonly observed in studies of wetting behavior on laser-irradiated surfaces immediately after laser treatment[**? ? ?**].

The difference in the estimated ECA between MD simulations and experimental results might be attributed to changes in surface chemistry immediately following laser irradiation. A wetting test on a laser-treated Ti surface is usually carried out in an open-air environment. Due to Ti's reactive nature, it tends to react with oxygen to form a thin layer of oxides, (as will be highlighted in the preceding paragraph) and also interacts with other environmental components. Upon exposure to atmospheric oxygen, Ti readily reacts to form a very thin layer of oxides on its surface. This oxide layer is often referred to as a passive oxide layer and primarily consists of compounds like titanium dioxide (TiO_2) and titanium oxides.

Additionally, the formation of this oxide layer changes the surface properties of Ti. It can affect surface energy as highlighted previously, chemical reactivity, and even the surface structure to some extent. Beyond oxygen, Ti oxide layer can interact with other environmental constituents present in the surrounding atmosphere. This interaction might involve gases, moisture, or other airborne particles. Furthermore, the presence of dirt particles, in the atmosphere during the experiment, could also contribute to these observed differences. The presence of dirt particles or contaminants in the environment can also influence the surface properties. These particles might adhere to the surface or react with the Ti or its oxide layer, altering the surface characteristics and potentially affecting the ECA.

It can also be observed from Table **??** that laser treatment increases the surface energy of the Ti system, influencing wettability. Interestingly, with an increase in surface energy, wettability tends to shift towards a more hydrophilic state, while lower surface energy favors hydrophilicity. This shift arises from changes in the surface texture of Ti induced by the laser, prompting the surface to repel water more effectively. However, surfaces with lower surface energy tend to favor hydrophilicity due to reduced interaction with water, resulting in less effective beading and increased spreading of the water nano-droplet on the surface, as depicted in Figure 7. The influence of surface energy and roughness induced by lasers on the spreading radius of water holds significant importance, particularly in the biomedical field. This impact is especially crucial in facilitating the osseointegration of osteoblasts, (i.e., the process by which living bone or tissues grow and attach themselves) onto artificial dental and orthopedic implants [14**?**].

As depicted in Figure 7, the dynamics of droplet spreading differ noticeably between the non-irradiated and laser-irradiated Ti surfaces. Specifically, the water nano-droplet demonstrates increased adherence to the laser-irradiated surface. From 0 ps to 100 ps, the spreading radius of the droplet exhibits linear growth, reaching approximately 5.5 nm. This signifies the initial stages of droplet spreading evident on both surfaces, illustrated in the evolution snapshots provided in Figure **??**. Beyond 100 ps, changes in the evolution of the spreading radius become apparent for both surfaces. Notably, the spreading radius of the non-irradiated Ti surpasses that of the laser-irradiated Ti by approximately 1 nm. However, in Figure **??**, the evolution appears subtle in the snapshots, primarily indicating changes in droplet shape with increasing timescale.

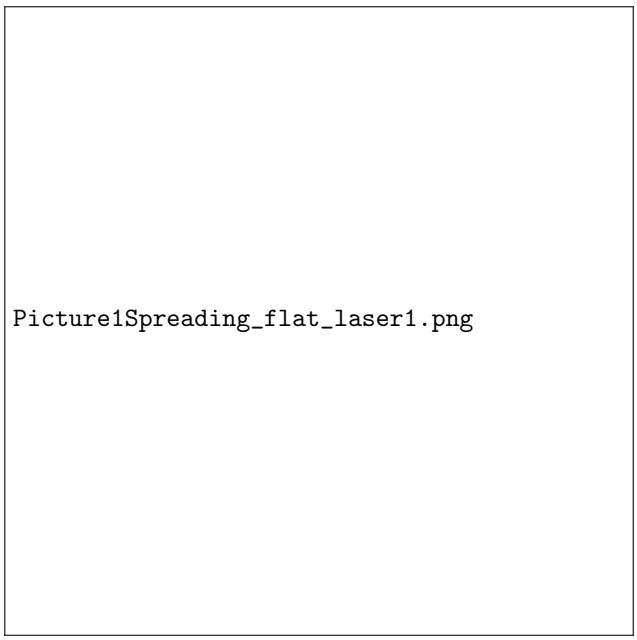

Figure 7: Spreading radius of water nanodroplet on non-irradiated and laser-irradiated titanium.

4 Conclusions

In summary, femtosecond laser surface treatment offers unparalleled advantages in terms of precision, minimal thermal damage, versatility, reduced post-processing requirements, rapid processing speed, and environmental friendliness. These advantages make femtosecond lasers an attractive choice for surface engineering applications across various industries, driving innovation and enabling the development of advanced functional materials with tailored properties.

The application of MD simulations offers a comprehensive understanding of the complex phenomena underlying the wettability modulation of femtosecond laser-treated Ti surfaces. By bridging the gap between theory and experiment, this study contributes to advancing our knowledge of surface engineering techniques and paves the way for the rational design of functional materials with tailored surface properties.

Acknowledgments

Here are the acknowledgments. Note the asterisk `\section*{Acknowledgments}` that signifies that this section is unnumbered.

References

[1] P. Dominic, D. Iabbaden, F. Bourquard, S. Reynaud, A. Nakhoul, A. Weck, J.-P. Colombier, and F. Garrelie, Unveiling nature and consequences of tungsten oxidation upon ultrafast laser irradiation, *Applied Surface Science* 159580 (2024).

[2] M. Prudent, D. Iabbaden, F. Bourquard, S. Reynaud, Y. Lefkir, A. Borroto, J.-F. Pierson, F. Garrelie, and J.-P. Colombier, High-density nanowells formation in ultrafast laser-irradiated thin film metallic glass, *Nano-micro letters* **14**, 103 (2022).

[3] P. Dominic, D. Iabbaden, F. Bourquard, S. Reynaud, A. Weck, J.-P. Colombier, and F. Garrelie, Ultrafast laser-induced sub-100 nm structures on tungsten surfaces: Stretched liquid dynamics insights, *physica status solidi (a)* 2300703 (2023).

[4] S. I. Anisimov, Electron emission from metal surfaces exposed to ultrashort laser pulses, *Sov. Phys. JETP* **39**, 3 (1975).

[5] S. Plimpton, Fast parallel algorithms for short-range molecular dynamics, *Journal of computational physics* **117**, 1 (1995).

[6] W. Yuan and T. Sizyuk, Ablation study in gold irradiated by single femtosecond laser pulse with electron temperature dependent interatomic potential and electron–phonon coupling factor, *Laser Physics* **31**, 036002 (2021).

[7] P. Hirel, Atomsk: A tool for manipulating and converting atomic data files, *Computer Physics Communications* **197**, 212 (2015).

[8] E. Bévillon, J.-P. Colombier, V. Recoules, and R. Stoian, Free-electron properties of metals under ultrafast laser-induced electron-phonon nonequilibrium: A first-principles study, *Physical Review B* **89**, 115117 (2014).

[9] Z. Lin, L. V. Zhigilei, and V. Celli, Electron-phonon coupling and electron heat capacity of metals under conditions of strong electron-phonon nonequilibrium, *Physical Review B* **77**, 075133 (2008).

[10] S. I. Anisimov and B. Rethfeld, in *Nonresonant Laser-Matter Interaction (NLMI-9)* (SPIE, 1997), vol. 3093, 192–203.

[11] C. Uher, in *Thermal conductivity: theory, properties, and applications* (Springer, 2004), 21–91.

[12] E. Bévillon, R. Stoian, and J.-P. Colombier, Nonequilibrium optical properties of transition metals upon ultrafast electron heating, *Journal of Physics: Condensed Matter* **30**, 385401 (2018).

[13] C. Schäfer, H. M. Urbassek, L. V. Zhigilei, and B. J. Garrison, Pressure-transmitting boundary conditions for molecular-dynamics simulations, *Computational Materials Science* **24**, 421 (2002).

[14] A. Cunha, A.-M. Elie, L. Plawinski, A. P. Serro, A. M. B. do Rego, A. Almeida, M. C. Urdaci, M.-C. Durrieu, and R. Vilar, Femtosecond laser surface texturing of titanium as a method to reduce the adhesion of staphylococcus aureus and biofilm formation, *Applied Surface Science* **360**, 485 (2016).

[15] M. I. Mendelev, T. Underwood, and G. Ackland, Development of an interatomic potential for the simulation of defects, plasticity, and phase transformations in titanium, *The Journal of chemical physics* **145**, 154102 (2016).

[16] A. Stukowski, Visualization and analysis of atomistic simulation data with ovito–the open visualization tool, *Modelling and simulation in materials science and engineering* **18**, 015012 (2009).

[17] A. C. Van Duin, S. Dasgupta, F. Lorant, and W. A. Goddard, Reaxff: a reactive force field for hydrocarbons, *The Journal of Physical Chemistry A* **105**, 9396 (2001).

[18] K. Chenoweth, A. C. Van Duin, and W. A. Goddard, Reaxff reactive force field for molecular dynamics simulations of hydrocarbon oxidation, *The Journal of Physical Chemistry A* **112**, 1040 (2008).

[19] T. P. Senftle, S. Hong, M. M. Islam, S. B. Kylasa, Y. Zheng, Y. K. Shin, C. Junkermeier, R. Engel-Herbert, M. J. Janik, H. M. Aktulga, et al., The reaxff reactive force-field: development, applications and future directions, *npj Computational Materials* **2**, 1 (2016).

[20] S.-Y. Kim, N. Kumar, P. Persson, J. Sofo, A. C. Van Duin, and J. D. Kubicki, Development of a reaxff reactive force field for titanium dioxide/water systems, *Langmuir* **29**, 7838 (2013).

[21] M. Raju, A. C. Van Duin, and K. A. Fichthorn, Mechanisms of oriented attachment of tio2 nanocrystals in vacuum and humid environments: reactive molecular dynamics, *Nano letters* **14**, 1836 (2014).

[22] X. Zhang and A. Bieberle-Hütter, Modeling and simulations in photoelectrochemical water oxidation: from single level to multiscale modeling, *ChemSusChem* **9**, 1223 (2016).

[23] P. Kofstad, High-temperature oxidation of titanium, *Journal of the Less Common Metals* **12**, 449 (1967).

[24] H. J. Berendsen, J. R. Grigera, and T. P. Straatsma, The missing term in effective pair potentials, *Journal of Physical Chemistry* **91**, 6269 (1987).